Electronic Supplementary Material (ESI) for Inorganic Chemistry Frontiers.
This journal is © the Partner Organisations 2024

Electronic Supporting Information

for

Hierarchical mesoporous N-doped carbon as Efficient ORR/OER bifunctional electrocatalyst for rechargeable zinc-air battery

Ping Li,[a,†] Jinghong Wen,[a,†] Yang Xiang,[a] Meiqi Li,[a] Yunxiu Zhao,[a] Suna Wang,[a] Jianmin Dou,[a] Yunwu Li,[*a,c] Huiyan Ma,[*a,c] and Liqiang Xu[*b]

[a] Shandong Provincial Key Laboratory of Chemical Energy Storage and Novel Cell Technology, and School of Chemistry and Chemical Engineering, Liaocheng University, Liaocheng, 252000, P. R. China.

[b] Key Laboratory of Colloid and Interface Chemistry, Ministry of Education, School of Chemistry and Chemical Engineering, Shandong University, Jinan, 250100, P. R. China.

[c] Key Laboratory of Advanced Energy Materials Chemistry (Ministry of Education), Nankai University, Tianjin, 300071, P. R. China.

Corresponding authors.

E-mail addresses: liyunwu@lcu.edu.cn; mahuiyanyan@163.com; xulq@sdu.edu.cn.

[†] These authors contributed equally to this work.

S1. Experimental section

S1.1. Chemicals

The ligand DCP was synthesized according to the literatures.[S1-S3] All the other chemicals were commercially purchased and used as received.

S1.2. Material characterization

The powder X-ray diffraction (PXRD) was obtained on a D/MAX-rA (Rigaku) diffractometer with Cu K_α radiation (λ = 1.542 Å) with a scan rate of 4°/min. Raman spectrum was tested using Monovista CRS500. X-ray photoelectron spectrums (XPS) were carried out using ESCALAB Xi+. N_2 adsorption experiment was tested using a Micrometrics ASAP 2020M. Electron microscopy measurements were measured using field-emission scanning electron microscopy (SEM, JSM-6360). Transmission electron microscopy (TEM) was measured by JEM-2100 at 200 kV.

S1.3. Electrochemical measurements

The electrocatalytic performance was tested using a Gamry references 3000 electrochemical workstation and a Pine electrode rotator. In this experiment, 3.2 mg NDC-800 catalyst (or 20% Pt/C) and 2.5 mg toner were dispersed in 570 μL pure H_2O and 177 μL ethanol, and then added with 3 μL 5wt.% Nafion to form a mixture. The mixture was ultrasonic for a period of time to disperse evenly. After that, 12 μL of the mixture were uniformly dripped onto the electrode. ORR tests were performed in a 70 mL 0.1 M KOH electrolyte using a three-electrode system. RDE (rotating disk electrode) glass carbon electrode as the working electrode, saturated Ag/AgCl as the reference electrode, platinum foil as the counter electrode. For comparison purposes, all potentials are relative to the reversible hydrogen electrode (RHE). The equation used is as follows:

$E_{RHE} = E_{Ag/AgCl} + 0.197\ V + 0.0591pH$

Koutecky-Levich (*K-L*) equations (research on ORR dynamics based on RDE data):

$$\frac{1}{J} = \frac{1}{J_K} + \frac{1}{J_L} = \frac{1}{J_K} + \frac{1}{B\omega^{1/2}} \quad (1a)$$

$B = 0.62nFC^*\ O2D2/3\ O2v^{-1/6}$

(1b)

$$J_K = nFkC^* \mathrm{O2} \quad (1c)$$

The equation of H_2O_2 yield and n was calculated from the RRDE (rotating ring disk electrode) data:

$$H_2O_2\% = \frac{2I_R/N}{I_D + I_R/N} \quad (2a)$$

$$n = \frac{4I_D}{I_D + I_R/N} \quad (2b)$$

In equation (1), J, J_L and J_K are the measured current density, diffusion limit current density and dynamic current density (mA cm^{-2}), respectively. B is the inverse of the slope from *K-L* plots. ω is RDE electrode rotating angular velocity (rad s^{-1}). n is the number of electrons transferred. F is Faraday's constant (96485 C mol^{-1}). $C^* O_2$ is the concentration of oxygen in the solution (1.2×10^{-6} mol cm^{-3}). D_{O_2} is the diffusion coefficient of O_2 in the electrolyte (1.9×10^{-5} cm^2 s^{-1}). v is the kinematic viscosity of electrolyte at room temperature (0.01 cm^2 s^{-1}). k is the electron transfer rate constant.

In equation (2), I_R is the ring current, I_D is the disk current, and N is the current collection efficiency of the Pt ring (0.37).

S1.4. Density functional theory (DFT) calculation

All calculations are performed with the VASP simulation package.[S4] The core electrons are treated with the Projector Augmented Wave (PAW) approach.[S5,S6] The Perdew, Burke and Ernzerhof (PBE) functional is adopted to calculate the exchange and correlation energy, as formulated in the generalized gradient approximation (GGA) of the density functional theory.[S7,S8] The Kohn-Sham valence states were expanded in a plane-wave basis set with a cutoff energy of 400 eV. For the Brillouin zone integration, a Monkhorst-Pack 3 × 3 × 1 mesh was used. The force threshold of all the relaxed atoms was set to 0.05 eV/Å. In all cases, at least 15 Å of empty space above the adsorbed species is considered to avoid interactions between the replicas of the slab model.

S2. Additional Figs in supporting information

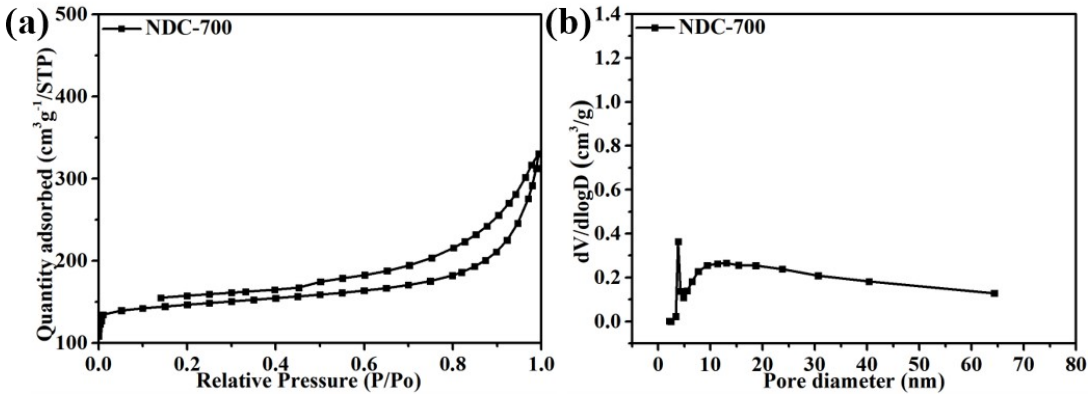

Fig. S1. (a) The N_2 sorption isotherm. (b) The pore size distribution curve of NDC-700.

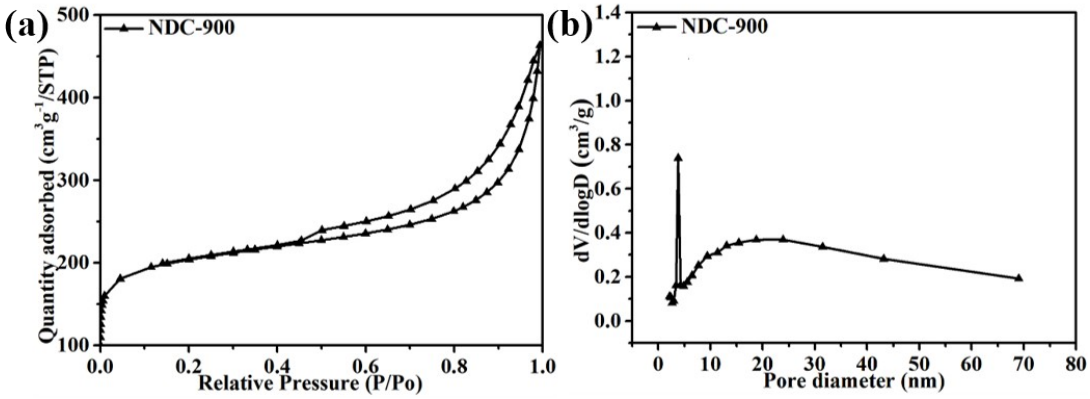

Fig. S2. (a) The N_2 sorption isotherm. (b) The pore size distribution curve of NDC-900.

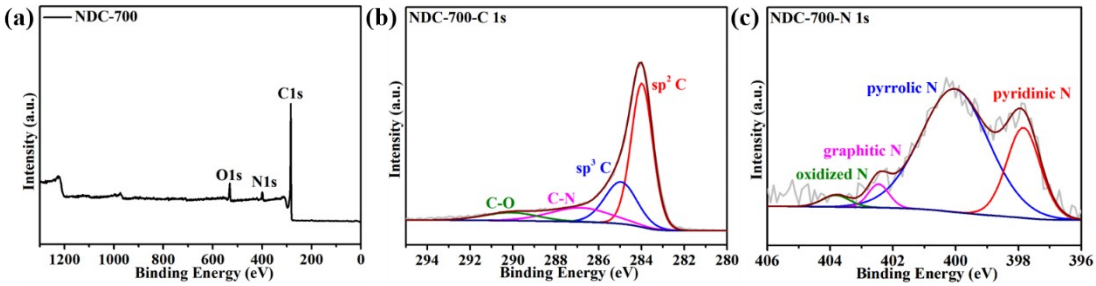

Fig. S3. (a) The XPS survey spectrum. (b, c) The XPS spectra of C 1s and N 1s of NDC-700.

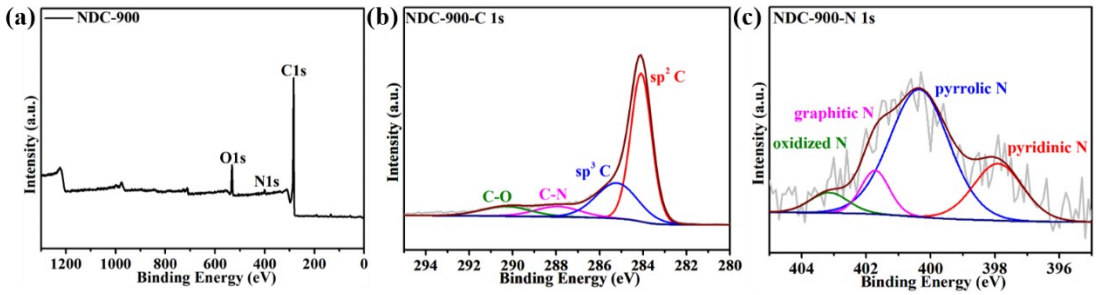

Fig. S4. (a) The XPS survey spectrum. (b, c) The XPS spectra of C 1s and N 1s of NDC-900.

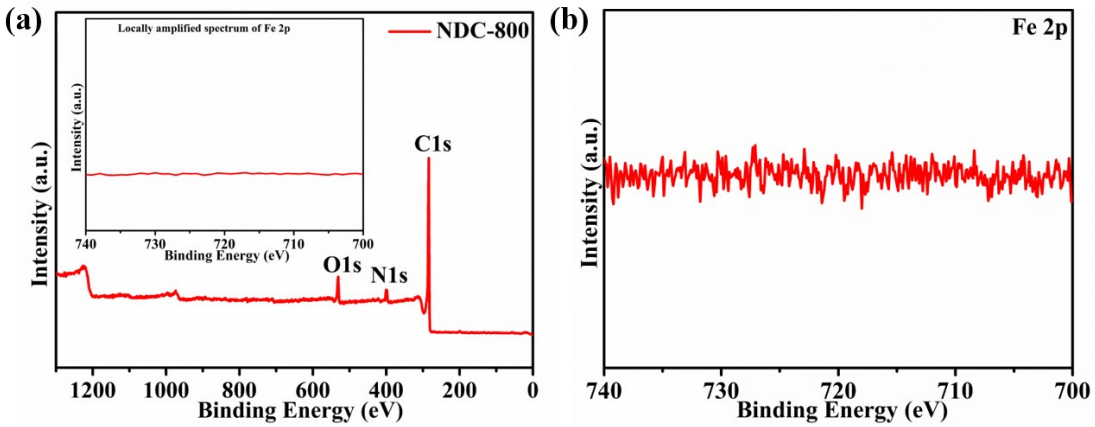

Fig. S5. (a) Locally amplified spectrum of Fe 2p in XPS full spectrum and (b) Fe 2p spectrum of NDC-800.

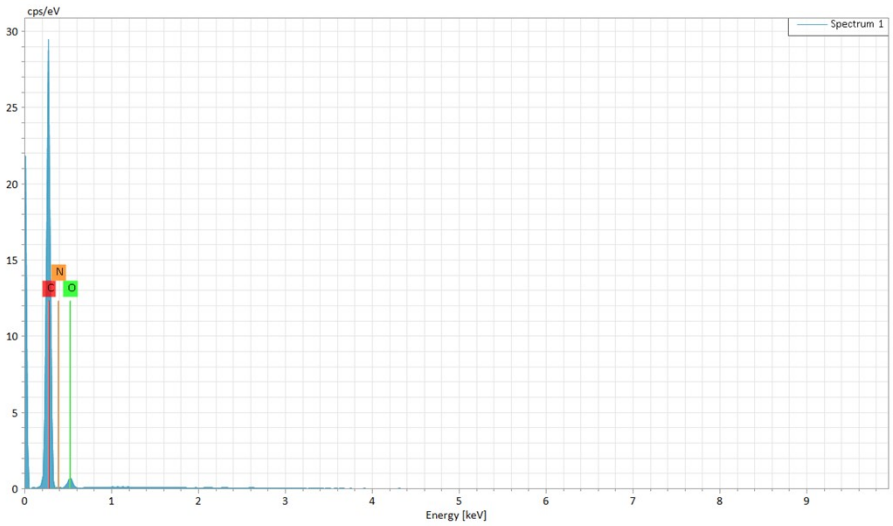

Fig. S6. EDS spectrum of NDC-800.

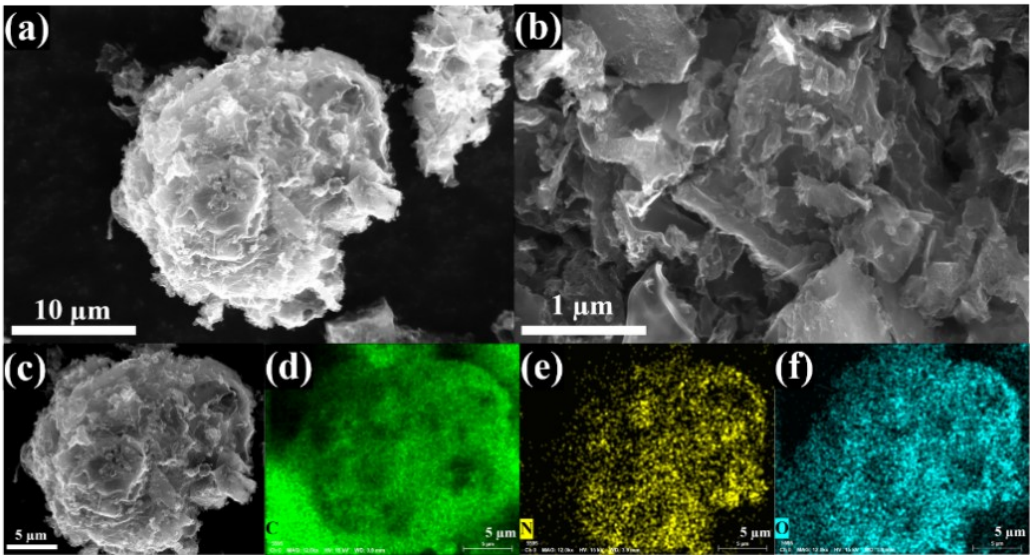

Fig. S7. (a-c) The SEM images of NDC-700 at different magnifications. (d-f) The EDS mapping images of selected regions: C, N and O.

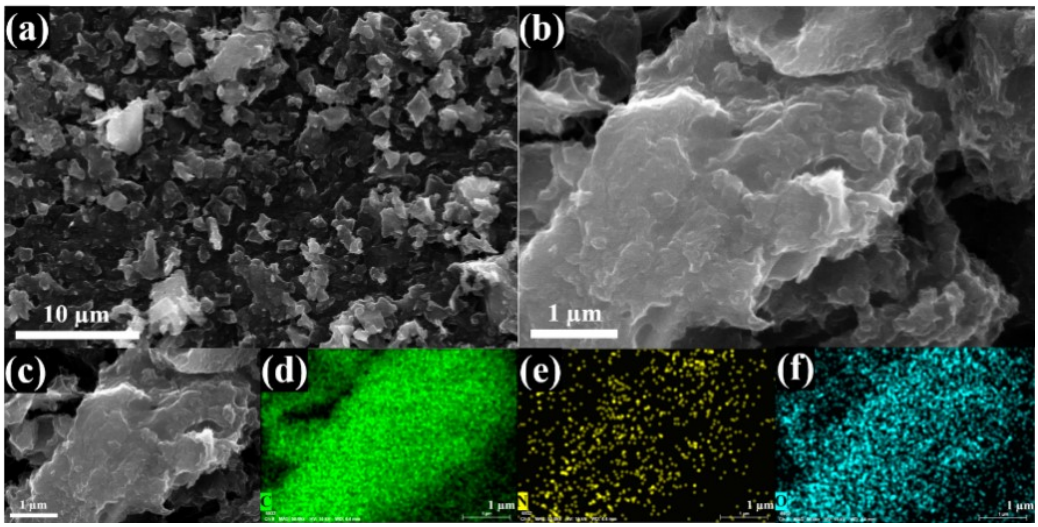

Fig. S8. (a-c) The SEM images of NDC-900 at different magnifications. (d-f) The EDS mapping images of selected regions: C, N and O.

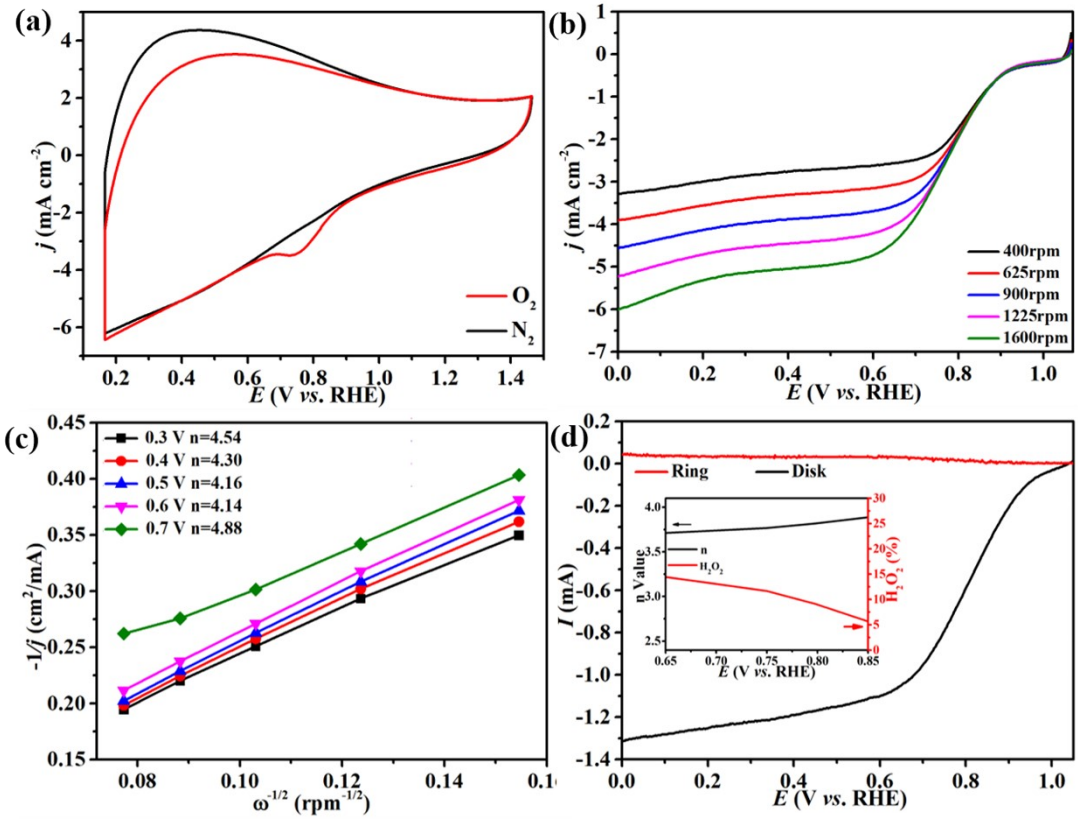

Fig. S9. (a) CV plots of the NDC-700 in O_2/N_2-saturated KOH solution (0.1 M). (b) ORR LSV curves of the NDC-700 catalyst. (c) *K-L* plots of the NDC-700 catalyst between potentials of 0.3 and 0.7 V. (d) RRDE polarization curves of NDC-700 catalyst at 1600 rpm (inset: extent of H_2O_2 yield and *n*).

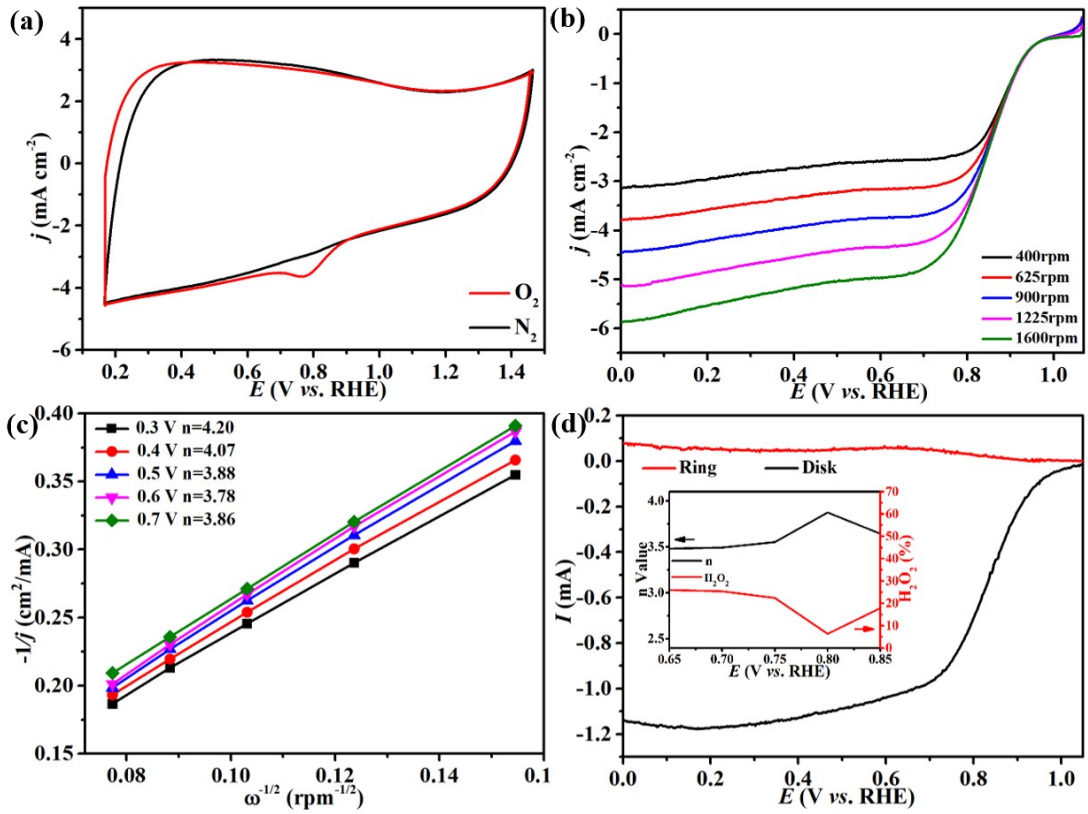

Fig. S10. (a) CV plots of the NDC-900 in O_2/N_2-saturated KOH solution (0.1 M). (b) ORR LSV curves of the NDC-900 catalyst. (c) *K-L* plots of the NDC-900 catalyst between potentials 0.3 and 0.7 V. (d) RRDE polarization curves of NDC-900 catalyst at 1600 rpm (inset: extent of H_2O_2 yield and *n*).

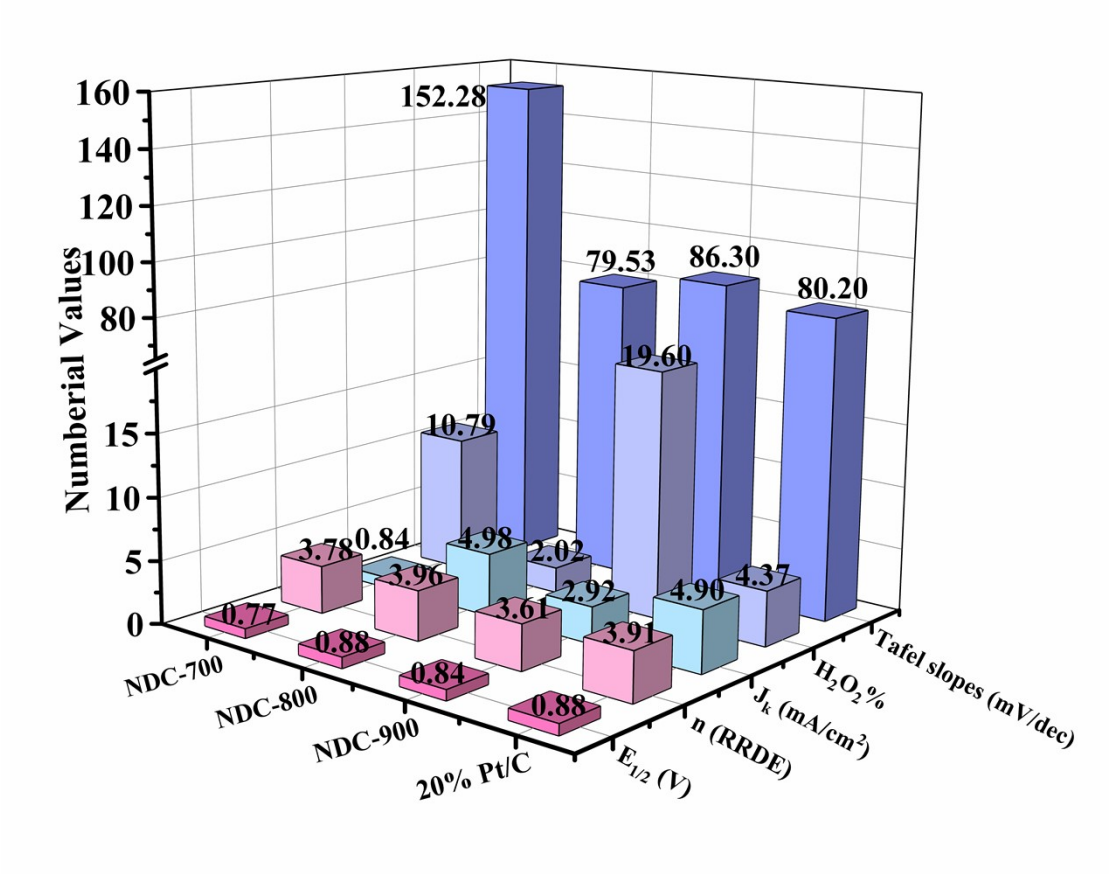

Fig. S11. Histogram of various ORR electrochemical evaluation parameters of NDC-700, NDC-800, NDC-900 and 20% Pt/C.

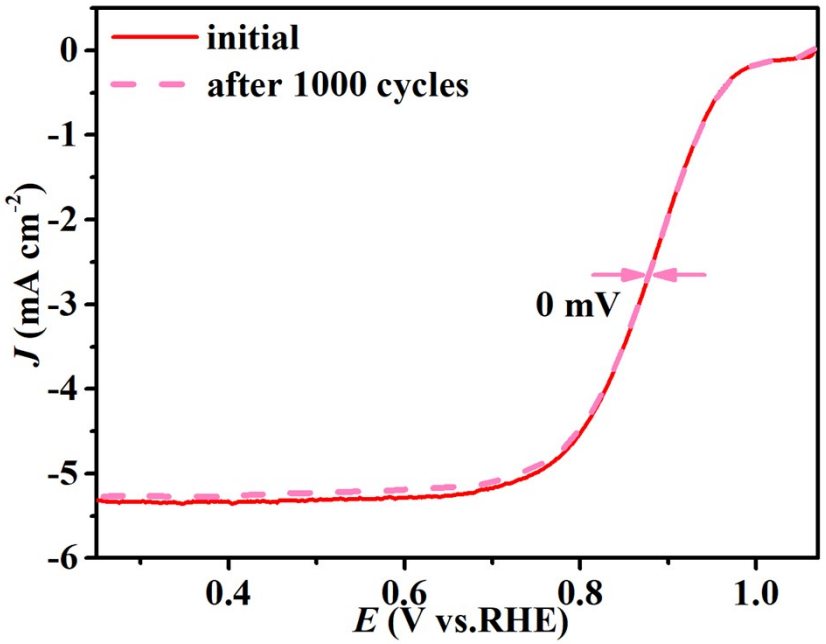

Fig. S12. (a) Polarization curves before and after 1000 cycles accelerated durability test (ADT) in 0.1 M KOH for ORR.

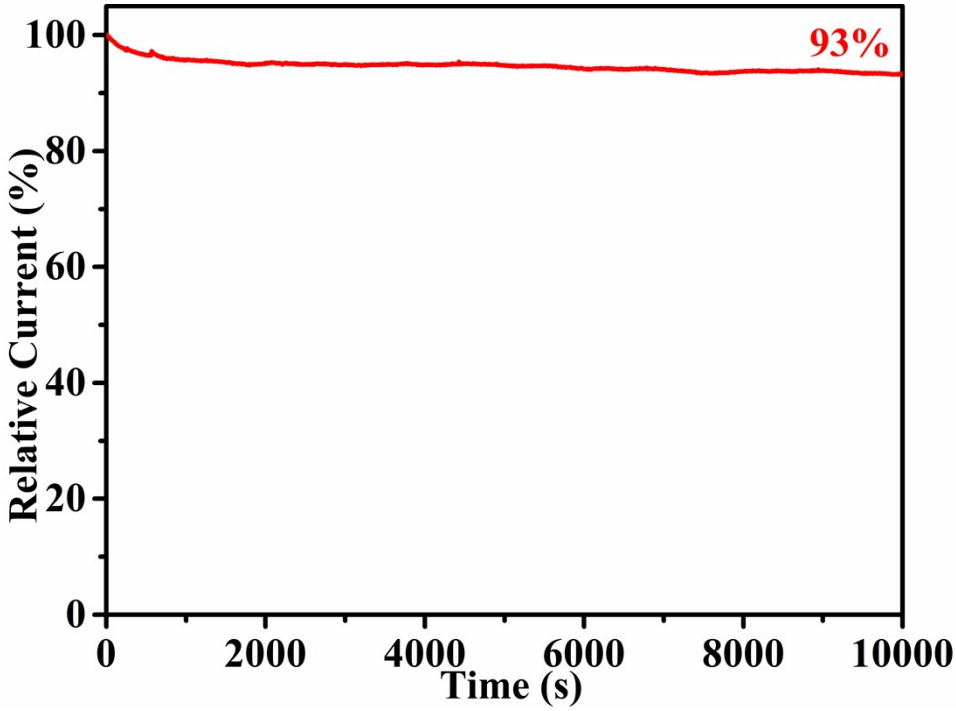

Fig. S13. OER stability of NDC-800 catalyst (*i-t* curve)**.**

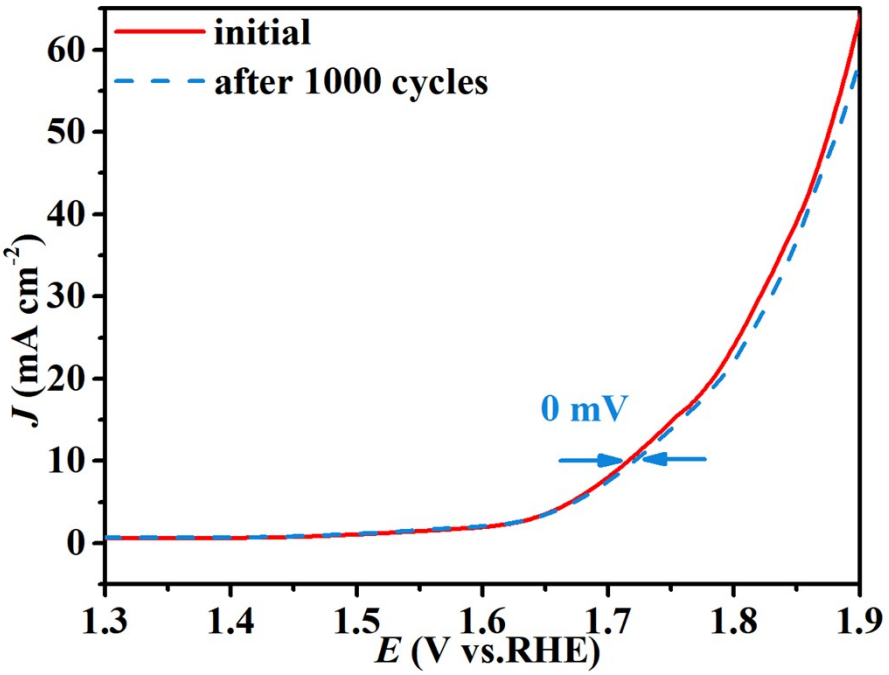

Fig. S14. (a) Polarization curves before and after 1000 cycles accelerated durability test (ADT) in 1.0 M KOH for OER.

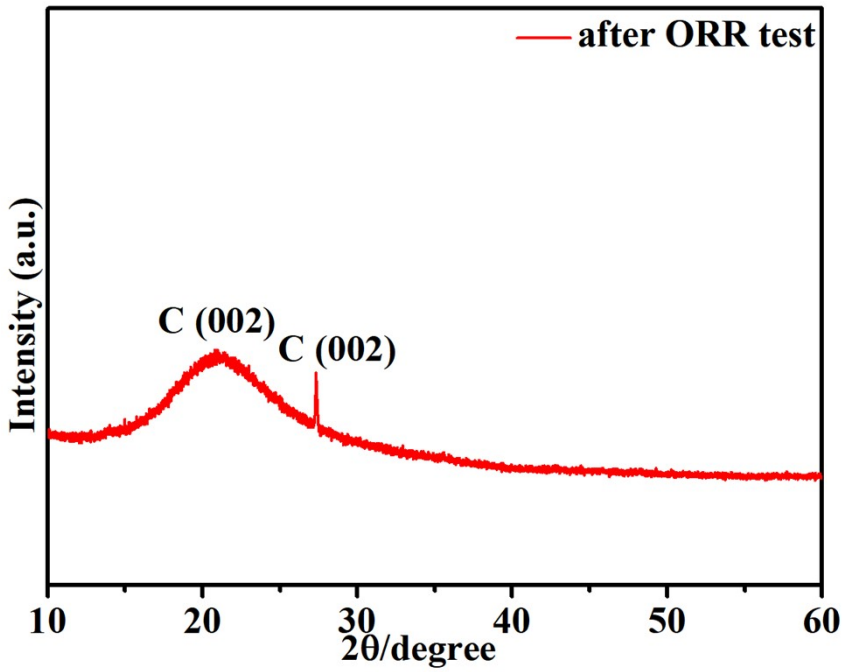

Fig. S15. PXRD patterns for NDC-800 catalyst after ORR stability test.

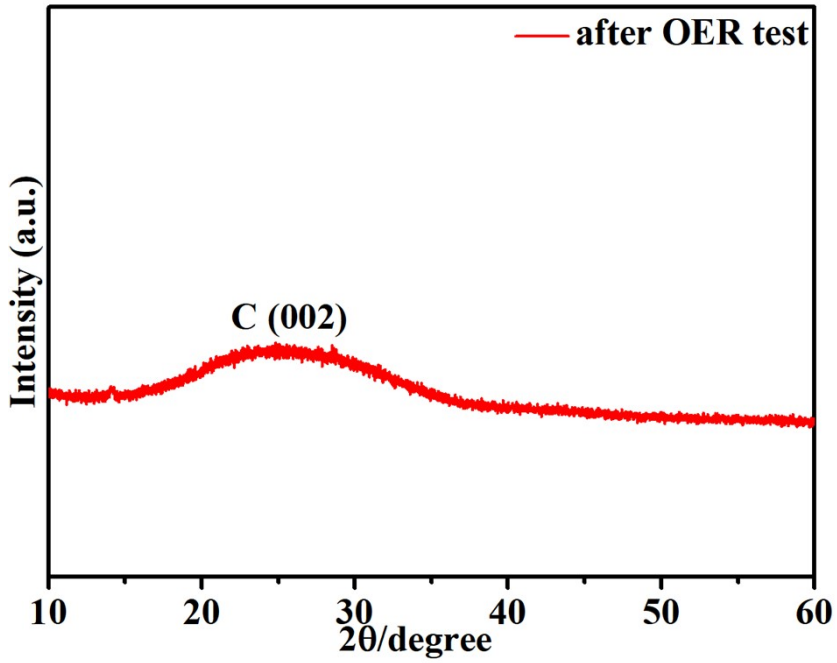

Fig. S16. PXRD patterns for NDC-800 catalyst after OER stability test.

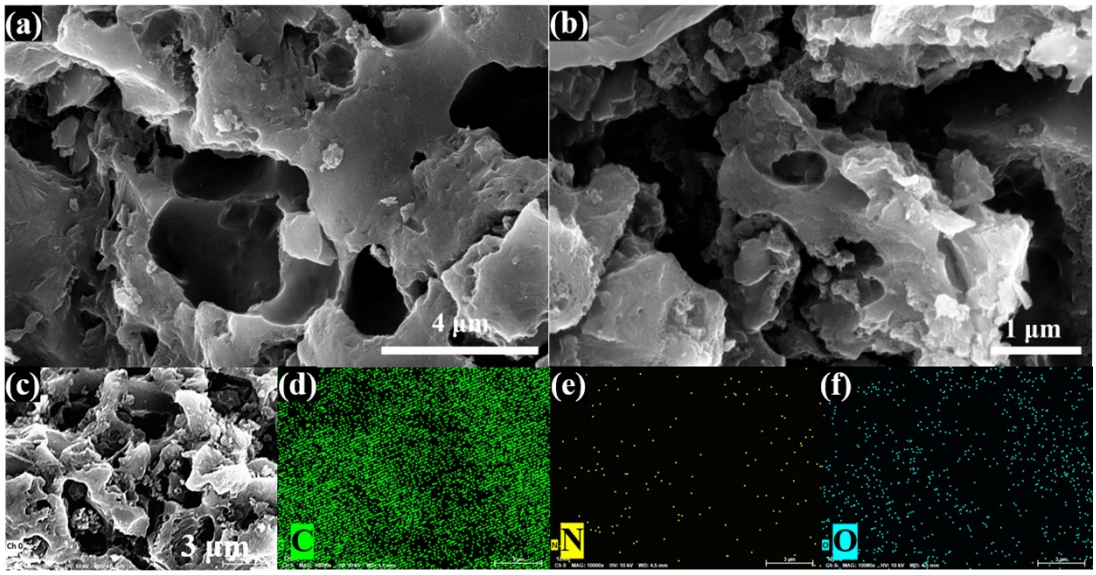

Fig. S17. (a-b) The SEM images at different magnifications. (c-f) The EDS mapping images of selected regions: C, N and O for NDC-800 catalyst after ORR stability test.

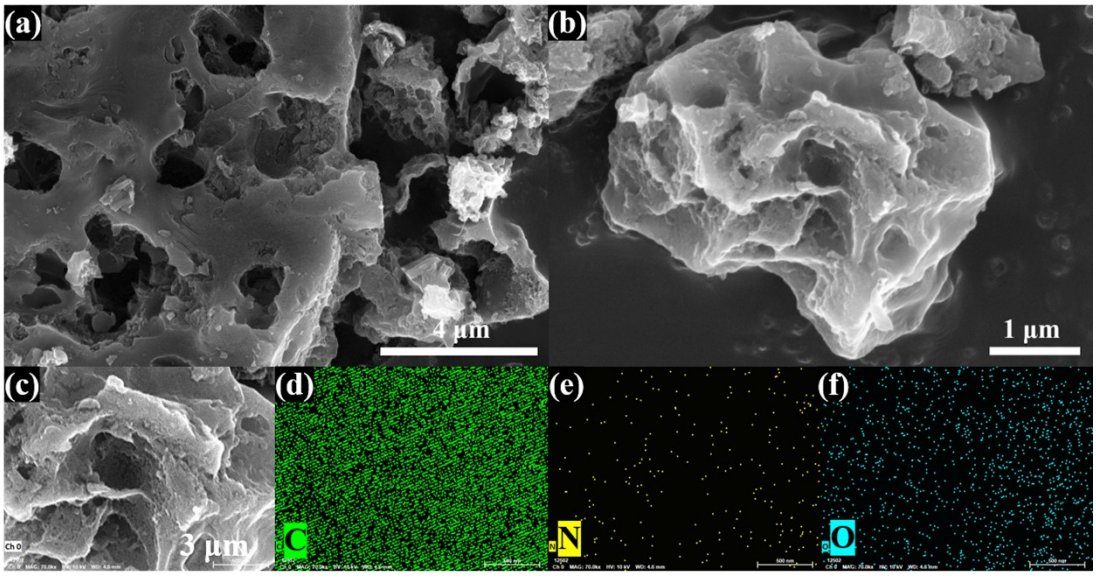

Fig. S18. (a-b) The SEM images at different magnifications. (c-f) The EDS mapping images of selected regions: C, N and O for NDC-800 catalyst after OER stability test.

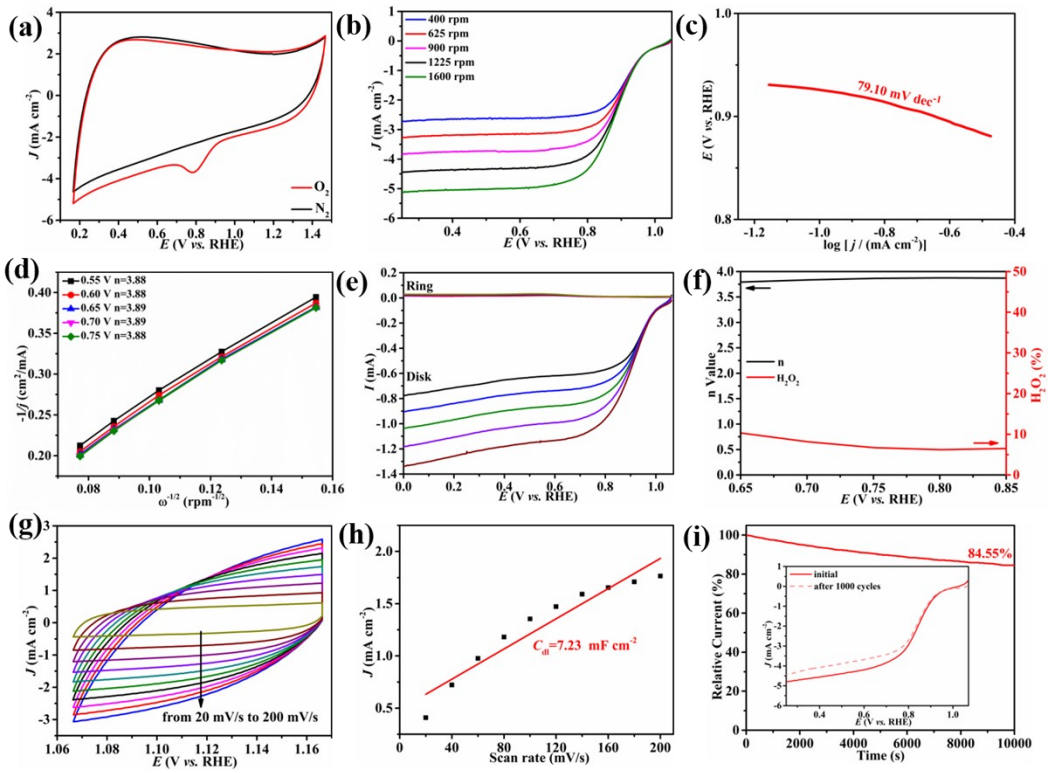

Fig. S19. The ORR performance using graphite rod as the counter electrode: (a) CV plots of the NDC-800 in O_2/N_2-saturated KOH solution (0.1 M). (b) ORR LSV curves of the NDC-800 catalyst at different speeds. (c) ORR Tafel slopes obtained from the LSV plots of NDC-800 catalyst (1600 rpm). (d) *K-L* plots of the NDC-800 catalyst between potentials of 0.55~0.75 V. (e) ORR polarization curves recorded on the RRDE of NDC-800 catalyst. (f) H_2O_2 yield and electron transfer number *n* from RRDE of NDC-800 catalyst. (g-h) The electrochemical double-layer capacitance (C_{dl}) of the three catalysts. (i) ORR stability of NDC-700, NDC-800, NDC-900 and 20% Pt/C catalysts.

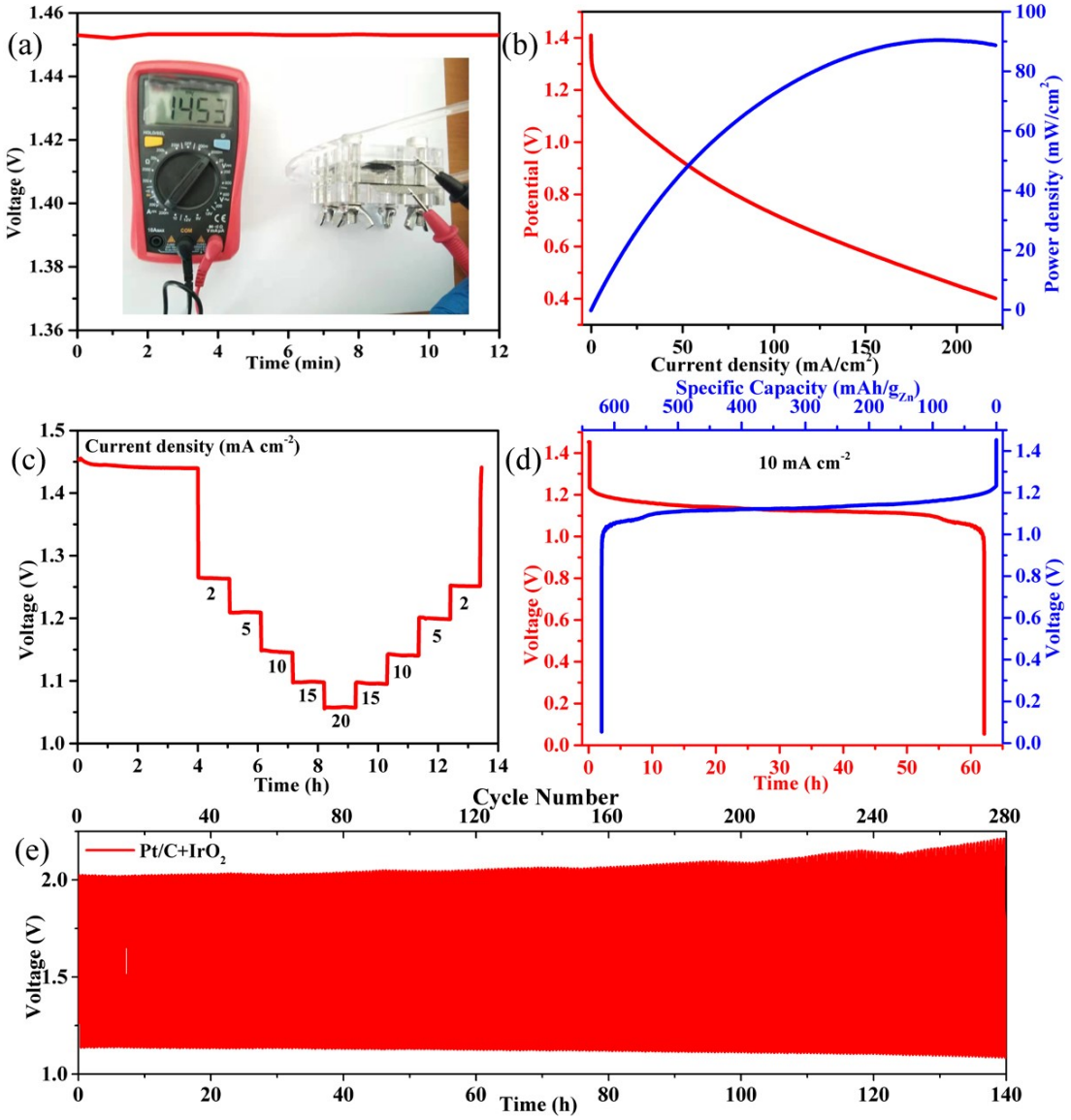

Fig. S20. The Zinc-air battery performance of a mixture containing two benchmark catalysts Pt/C+IrO_2/C (1:1): (a) The OCV plot of the Zinc-air battery (inset: OCV photograph). (b) Polarization plot and power density plot of the Zinc-air battery. (c) The rate capability of the Zinc-air battery under different current densities. (d) Galvanostatic discharge plot and corresponding specific capacity of the Zinc-air battery under 10 mA cm^{-2}. (e) The charge-discharge cycling stability curve at 2 mA cm^{-2} for 140 h.

S3. Additional tables in supporting information

Table S1. ICP-MS analysis of Fe element in NDC-800 and DCP-800.

Sample	Intensity (ppb)	wt.%
NDC-800	1.2015	0.03%
DCP-800	1.2011	0.03%

Table S2. The element quantity of NDC-700, NDC-800, and NDC-900 catalysts determined by XPS.

Samples	C(At %)	N(At %)	O(At %)
NDC-700	87.37	5.40	7.23
NDC-800	86.57	5.27	8.18
NDC-900	92.93	1.37	5.70

Table S3. Various C contents of NDC-700, NDC-800, and NDC-900 catalysts in C 1s analysis (relative to the percentage of C).

Samples	sp^2 C(At %)	sp^3 C(At %)	sp^3 C/sp^2 C
NDC-700	24.20	5.44	0.23
NDC-800	47.30	22.93	0.48
NDC-900	55.14	21.46	0.39

Table S4. The various N contents, the pyridinic N and graphinic N/total N ratios of NDC-700, NDC-800, and NDC-900 catalysts in N 1s analysis (relative to N percentage).

Samples	graphitic N (At %)	pyridinic N (At %)	pyridinic N and graphitic N/total N (%)
NDC-700	0.18	1.74	35.56
NDC-800	0.96	1.76	51.61
NDC-900	0.02	0.33	25.69

Table S5. Comparison of ORR performances of N-doped carbon in this work and the recently reported highly active metal-free carbons and transition-metal oxide bifunctional catalysts.

Catalysts	E_{onset} (V)	$E_{1/2}$ (V)	*n*	References
NDC-800	1.03	0.88	3.96	This work
N-GRW	0.92	0.84	--	S9
N-MG-800	0.94	0.835	3.94	S10
Co-doped np-graphene	0.987	0.845	3.9	S11
BNC-1000-3	0.95	0.83	3.7	S12
NPS-1&10&2	0.948	0.862	3.82-3.96	S13
ACTF-α-900	0.96	0.86	3.64 to 3.72	S14
N, P co-doped carbons	0.88	0.81	-	S15
Thiophene-sulfur covalent organic frameworks (MFTS-COFs)	0.82	0.70	3.81	S16

Table S6. The ECSA of NDC-700, NDC-800 and NDC-900 catalysts.

Catalysts	ECSA (cm^2)
NDC-700	29.40
NDC-800	34.79
NDC-900	33.17

Table S7. The ΔE parameters of N-doped carbon catalysts in this work and the recently reported references.

Catalysts	ΔE (V)	References
NDC-800	0.76	This work
NCN-1000-5	0.81	S17
NFPC-1100	0.86	S18
NS-CD@gf_a900	0.82	S19
Defective graphene	0.84	S20
CNIS-NC-CCC	0.78	S21
NCP-950	0.72	S22
CNRs-C	0.75	S23
N-doped graphene@SWCNT	1.00	S24
N-CN9	0.98	S25
NKCNPs	0.92	S26
N-PC@G-0.02	0.83	S27

Table S8. Comparison of Zn-air batteries performance assembled by various carbon materials.

Catalysts	Peak power density (mW cm^{-2})@*j* ($mA\ cm^{-2}$)	Specific capacity (mAh g_{Zn}^{-1})@*j* ($mA\ cm^{-2}$)	Durability @*j* ($mA\ cm^{-2}$)	References
NDC-800	186.12	630@10	60 h (120 cycles)@10	This work
N, P co-doped mesoporous nanocarbon	55@70	735@5	30 h@2	S28
N, O-codoped graphene	119	-	30 h@10	S29
N, F, P tri-doped carbon nanofibers	--	520@10	200 cycles	S30
N-doped carbon flake arrays grown on carbon nanofibers	--	530.17@6.25	90 cycles	S31
N and P co-doped carbon spheres	79	684@2	56 h@2	S32
CC-AC	52.3	--	1000 min	S33

References

S1 T. Y. Gu, M. Dai, D. J. Young, Z. G. Ren and J. P. Lang, Luminescent Zn(II) coordination polymers for highly selective sensing of Cr(III) and Cr(VI) in water, *Inorg. Chem.*, 2017, **56**, 4668-4678.

S2 Q. Tang, S. X. Liu, Y. W. Liu, J. Miao, S. J. Li, L. Zhang, Z. Shi and Z. P. Zheng, Cation sensing by a luminescent metal-organic framework with multiple lewis basic sites, *Inorg. Chem.*, 2013, **52**, 2799-2801.

S3 Z. M. Hao, X. Z. Song, M. Zhu, X. Meng, S. N. Zhao, S. Q. Su, W. T. Yang, S. Y. Song and H. J. Zhang, One-Dimensional Channel-Structured Eu-MOF for Sensing Small Organic Molecules and Cu^{2+} ion, *J. Mater. Chem. A*, 2013, **1**, 11043-11050.

S4 G. Kresse and J. Furthmüller, Efficiency of Ab-Initio Total Energy Calculations for Metals and Semiconductors Using a Plane-Wave Basis Set, *J. Comput. Mater. Sci.*, 1996, **6**, 15-50.

S5 P. E. Blöchl, Projector Augmented-Wave Method, *Phys. Rev. B*, 1994, **50**, 17953-17979.

S6 G. Kresse and D. Joubert, From Ultrasoft Pseudopotentials to the Projector Augmented-Wave Method, *Phys. Rev. B*, 1999, **59**, 1758-1775.

S7 J. P. Perdew, K. Burke and M. Ernzerhof, Generalized Gradient Approximation Made Simple, *Phys. Rev. Lett.*, 1996, **77**, 3865.

S8 J. P. Perdew, K. Burke and M. Ernzerhof, Erratum: Generalized Gradient Approximation Made Simple, *Phys. Rev. Lett*., 1997, **78**, 1396.

S9 H. B. Yang, J. W. Miao, S. F. Hung, J. Z. Chen, H. B. Tao, X. Z. Wang, L. P. Zhang, R. Chen, J. J. Gao, H. M. Chen, L. M. Dai and B. Liu, Identification of Catalytic Sites for Oxygen Reduction and Oxygen Evolution in N-Doped Graphene Bifunctional Electrocatalysts, *Sci. Adv.*, 2016, **2**, e1501122.

S10 J. H. Han, G. Huang, Z. L. Wang, Z. Lu, J. Du, H. Kashani and M. W. Chen, Low-Temperature Carbide-Mediated Growth of Bicontinuous Nitrogen-Doped Mesoporous Graphene as an Efficient Oxygen Reduction Electrocatalyst, *Adv. Mater.*, 2018, **30**, 1803588.

S11 H. J. Qiu, P. D, K. L. Hu, J. J. Gao, H. L. Li, P. Liu, T. Ina, K. Ohara, Y. Ito and M. W. Chen, Metal and Nonmetal Codoped 3D Nanoporous Graphene for

Efficient Bifunctional Electrocatalysis and Rechargeable Zn-Air Batteries, *Adv. Mater.*, 2019, **31**, 1900843.

S12 W. S. Li, Z. Y. Sun, J. M. Yang, G. Y. Huang and H. B. Zhu, Efficient Metal-Free ZIF-8 Derived B,N-Codoped Carbon Electrocatalyst toward Oxygen Reduction, *Z. Anorg. Allg. Chem*., 2021, **647**, 1326-1333.

S13 Y. D. Long, F. H. Ye, L. Shi, X. N. Lin, R. Paul, D. Liu and C. G. Hu, N, P, and S Tri-Doped Holey Carbon as an Efficient Electrocatalyst for Oxygen Reduction in Whole pH Range for Fuel Cell and Zinc-Air Batteries, *Carbon*, 2021, **179**, 365-376.

S14 N. N. Li, R. Z. Tang, Y. Z. Su, C. B. Lu, Z. M. Chen, J. Sun, Y. Q. Lv, S. Han, C. Q. Yang and X. D. Zhuang, Isometric Covalent Triazine Frameworks Derived Porous Carbons as Efficient Metal-Free Electrocatalysts for Oxygen Reduction Reactions, *ChemSusChem*, 2023, **16**, e202201937.

S15 C. Yang, S. S. Tao, N. Huang, X. B. Zhang, J. G. Duan, R. Makiura and S. Maenosono, Heteroatom-Doped Carbon Electrocatalysts Derived from Nanoporous Two-Dimensional Covalent Organic Frameworks for Oxygen Reduction and Hydrogen Evolution, *ACS Appl. Nano Mater.*, 2020, **3**, 5481-5488.

S16 D. H. Li, C. Y. Li, L. J. Zhang, H. Li, L. K. Zhu, D. J. Yang, Q. R. Fang, S. L. Qiu and X. D. Yao, Metal-Free Thiophene-Sulfur Covalent Organic Frameworks: Precise and Controllable Synthesis of Catalytic Active Sites for Oxygen Reduction, *J. Am. Chem. Soc*., 2020, **142**, 8104-8108.

S17 H. Jiang, J. X. Gu, X. S. Zheng, M. Liu, X. Q. Qiu, L. B. Wang, W. Z. Li, Z. F. Chen, X. B. Ji and J. Li, Defect-Rich and Ultrathin N Doped Carbon Nanosheets as Advanced Trifunctional Metal-free Electrocatalysts for the ORR, OER and HER, *Energy Environ. Sci.*, 2019, **12**, 322-333.

S18 Y. N. Sun, J. Q. Yang, X. S. Ding, W. Y. Ji, A. Jaworski, N. Hedin and B. Han, Synergetic Contribution of Nitrogen and Fluorine Species in Porous Carbons as Metal-free and Bifunctional Oxygen Electrocatalysts for Zinc-air Batteries, *Appl. Catal. B Environ.*, 2021, **297**, 120448.

S19 J. H. Shin, J. Guo, T. T. Zhao and Z. X. Guo, Functionalized Carbon Dots on Graphene as Outstanding Non-Metal Bifunctional Oxygen Electrocatalyst, *Small*, 2019, **15**, 1900296.

S20 Y. Jia, L. Z. Zhang, A. J. Du, G. P. Gao, J. Chen, X. C. Yan, C. L. Brown and X.

D. Yao, Defect Graphene as a Trifunctional Catalyst for Electrochemical Reactions, *Adv. Mater.*, 2016, **28**, 9532-9538.

S21 X. J. Zheng, Y. H. Qian, H. Y. Gong, W. H. Shi, J. Yan, W. T. Wang, X. M. Guo, J. H. Zhang, X. C. Cao and R. Z. Yang, Bridge-Linking Interfacial Engineering of Triple Carbons for Highly Efficient and Binder-Free Electrodes toward Flexible Zn-Air Batteries, *Appl. Catal. B Environ.*, 2022, **319**, 121937.

S22 Z. J. Li, S. Q. Ji, H. X. Liu, C. Xu, C. M. Guo, X. Lu, H. X. Sun, S. Dou, S. X. Xin, J. H. Horton and C. He, Constructing Asymmetrical Coordination Microenvironment with Phosphorus-Incorporated Nitrogen-Doped Carbon to Boost Bifunctional Oxygen Electrocatalytic Activity, *Adv. Funct. Mater.*, 2024, **34**, 2314444.

S23 D. P. Xue, Y.Y. Guo, B. Lu, H. C. Xia, W. F. Yan, D. F. Xue, S. C. Mu and J. N. Zhang, Monomicelle-Directed Engineering of Strained Carbon Nanoribbons as Oxygen Reduction Catalyst, *Adv. Sci.*, 2023, **10**, 2302930.

S24 G. L.Tian, M. Q. Zhao, D. S. Yu, X. Y. Kong, J. Q. Huang, Q. Zhang and F. Wei, Nitrogen-Doped Graphene/Carbon Nanotube Hybrids: In Situ Formation on Bifunctional Catalysts and Their Superior Electrocatalytic Activity for Oxygen Evolution/Reduction Reaction, *Small*, 2014, **10**, 2251-2259.

S25 C. Zhang, G. X. Zhang, H. Y. Li, Y. N. Chang, Z. Chang, J. F. Liu and X. M. Sun, Interfacial Dehalogenation-Enabled Hollow N-Doped Carbon Network as Bifunctional Catalysts for Rechargeable Zn-Air Battery. *Electrochim. Acta.*, 2017, **247**, 1044-51.

S26 Q. C. Wang, Y. P. Lei, Y. G. Zhu, H. Wang, J. Z. Feng, G. Y. Ma, Y. D. Wang, Y. J. Li, B. Nan, Q. G. Feng, Z. G. Lu and H. Yu, Edge Defect Engineering of Nitrogen-Doped Carbon for Oxygen Electrocatalysts in Zn-Air Batteries, *ACS Appl. Mater. Interfaces*, 2018, **10**, 29448-29456.

S27 S. W. Liu, H. M. Zhang, Q. Zhao, X. Zhang, R. R. Liu, X. Ge, G. Z. Wang, H. J. Zhao and W. P. Cai, Metal-Organic Framework Derived Nitrogen-Doped Porous Carbon@Graphene Sandwich-Like Structured Composites as Bifunctional Electrocatalysts for Oxygen Reduction and Evolution Reactions, *Carbon*, 2016, **106**, 74-83.

S28 J. T. Zhang, Z. H. Zhao, Z. H. Xia and L. M. Dai, A Metal-Free Bifunctional Electrocatalyst for Oxygen Reduction and Oxygen Evolution Reactions, *Nat. Nanotechnol.*, 2015, **10**, 444-452.

S29 Q. Hu, G. M. Li, G. D. Li, X. F. Liu, B. Zhu, X. Y. Chai, Q. L. Zhang, J. H. Liu and C. X. He, Trifunctional Electrocatalysis on Dual-Doped Graphene Nanorings-Integrated Boxes for Efficient Water Splitting and Zn-Air Batteries, *Adv. Energy Mater.*, 2019, **9**, 1803867.

S30 M. G. Wu, Y. Q. Wang, Z. X. Wei, L. Wang, M. Zhuo, J. T. Zhang, X. P. Han and J. M. Ma, Ternary Doped Porous Carbon Nanofibers with Excellent ORR and OER Performance for Zinc-Air Batteries, *J. Mater. Chem. A*, 2018, **6**, 10918-10925.

S31 D. X. Ji, L. Fan, L. L. Li, S. J. Peng, D. S. Yu, J. N. Song, S. Ramakrishna and S. J. Guo, Atomically Transition Metals on Sel-Supported Porous Carbon Flake Arrays as Binder-Free Air Cathode for Wearable Zinc-Air Batteries, *Adv. Mater.*, 2019, **31**, 1808267.

S32 S. Chen, L. L. Zhao, J. Z. Ma, Y. Q. Wang, L. M. Dai and J. T. Zhang, Edge-Doping Modulation of N,P-Codoped Porous Carbon Spheres for High-Performance Rechargeable Zn-Air Batteries, *Nano Energy*, 2019, **60**, 536-544.

S33 K. Kordek, L. X. Jiang, K. C. Fan, Z. J. Zhu, L. Xu, M. Al-Mamun, Y. H. Dou, S. Chen, P. R. Liu, H. J. Yin, P. Rutkowski and H. J. Zhao, Two-Step Activated Carbon Cloth with Oxygen-Rich Functional Groups as a High-Performance Additive-Free Air Electrode for Flexible Zinc-Air Batteries, *Adv. Energy Mater.*, 2018, **9**, 1802936.